Article:
Palmer, C. A.J., Campbell, P. T., Ma, Y. et al. (18 more authors) (2019) Field reconstruction from proton radiography of intense laser driven magnetic reconnection. Physics of Plasmas. 083109. ISSN 1089-7674

https://doi.org/10.1063/1.5092733

Field reconstruction from proton radiography of intense laser driven magnetic reconnection

C. A. J. Palmer[1,†], P. T. Campbell[2], Y. Ma[2,†], L. Antonelli[3], A. F. A. Bott[1], G. Gregori[1], J. Halliday[4], Y. Katzir[5], P. Kordell[2], K. Krushelnick[2], S. V. Lebedev[4], E. Montgomery[5], M. Notley[5], D. C. Carroll[5], C. P. Ridgers[3], A. A. Schekochihin[1], M. J. V. Streeter[4,†], A. G. R. Thomas[2,†], E. R. Tubman[4], N. Woolsey[3], and L. Willingale[2,†]

[1] *Clarendon Laboratory, University of Oxford, Parks Road, Oxford, OX1 3PU, United Kingdom*

[2] *Center for Ultrafast Optical Science, University of Michigan, 2200 Bonisteel Boulevard, Ann Arbor, Michigan 48109, USA*

[3] *Department of Physics, York Plasma Institute, University of York, York YO10 5DD, United Kingdom*

[4] *Blackett Laboratory, Imperial College London, SW7 2BZ, United Kingdom and*

[5] *Central Laser Facility, STFC Rutherford-Appleton Laboratory, Chilton, Didcot, Oxfordshire, OX11 0QX, United Kingdom*

(Dated: July 24, 2019)

Magnetic reconnection is a process that contributes significantly to plasma dynamics and energy transfer in a wide range of plasma and magnetic field regimes, including inertial confinement fusion experiments, stellar coronae and compact, highly magnetized objects like neutron stars. Laboratory experiments in different regimes can help refine, expand and test the applicability of theoretical models to describe reconnection. Laser-plasma experiments exploring magnetic reconnection at moderate intensities ($I_L \sim 10^{14}$ Wcm^{-2}) have been performed previously, where the Biermann battery effect self-generates magnetic fields and the field dynamics studied using proton radiography. At high laser intensities ($I_L\lambda_L^2 > 10^{18}$ Wcm$^{-2}\mu$m^2), relativistic surface currents and the time-varying electric sheath fields generate the azimuthal magnetic fields. Numerical modeling of these intensities has shown the conditions within the magnetic field region can reach the threshold where the magnetic energy can exceed the rest mass energy such that $\sigma_{cold} = B^2/(\mu_0 n_e m_e c^2) > 1$ [A. E. Raymond, *et al.*, Phys. Rev. E, **98**, 043207 (2018)]. Presented here is the analysis of the proton radiography of a high-intensity ($\sim 10^{18}$ Wcm^{-2}) laser driven magnetic reconnection geometry. The path integrated magnetic fields are recovered using a "field-reconstruction algorithm" to quantify the field strengths, geometry and evolution.

PACS numbers:

I. INTRODUCTION

Magnetic reconnection is a fundamental process where magnetic field lines break and reconfigure in a lower energy state, thereby releasing energy to heat the plasma. It is an important mechanism in many astrophysical situations, such as powering coronal mass ejections and solar flares, the solar wind interacting with the Earth's magnetic fields [1], as well as in the universe's most violent and energetic objects like pulsars [2], active galactic nuclei [3] or gamma ray bursts [4]. Direct measurements of the fields and particles are either difficult in the case of the near-Earth environment [5], or impossible at greater distances. Furthermore, these phenomena cover a wide range of plasma parameters and field conditions making the topic diverse. Studying reconnection processes in the laboratory is therefore a valuable method for enhancing our theoretical knowledge.

Terrestrially, magnetic reconnection can occur within tokamak plasma [6], or dedicated magnetic reconnection experiments such as the MRX machine [7]. Over the last decade, laser-driven magnetic reconnection experiments have been developed using high-energy nanosecond laser pulses where self-generated magnetic fields are driven together by the plasma flow [8–15]. At intensities of $\sim 10^{14}$ Wcm^{-2}, a laser pulse can heat a target to form a plasma containing non-parallel temperature and density gradients, thus generating azimuthal magnetic fields through the Biermann battery [16–18]. The megagauss-strength magnetic fields are transported by the bulk plasma motion at the plasma sound speed, $c_s = (Zk_BT_e/m_i)^{1/2}$ where Z and m_i are the ion charge and mass respectively and k_BT_e is the electron temperature; this is described as "frozen-in-flow". Focusing two laser pulses onto a target in close proximity produces a geometry where two opposing direction magnetic fields are driven into one another in the midplane. Fox *et al.* found in this strongly driven reconnection regime the compression of the magnetic flux means the Alfvén speed is time dependent [19], an important consideration for understanding the reconnection rate.

Increasing the laser intensity generates hotter electrons. The inverse-velocity dependence of the collision operator means the mean-free-path for the hottest electrons is large compared with the system size. Therefore, Braginskii's collisional transport theory breaks down and kinetic effects become important so that heat flows are "non-local". The magnetic field can then travel faster than the ion fluid velocity [20–22]. Driving a magnetic reconnection under these conditions means the reconnection rates are dictated by heat flows rather than the Alfvènic flows [23].

At intensities of $I\lambda_\mu^2 > 1.4 \times 10^{18}$ Wcm^{-2}, where λ_μ is the laser wavelength in micrometers, the electrons are

accelerated to velocities approaching the speed of light and their motion can generate an azimuthal magnetic field [24–28]. These relativistic electrons rapidly expand from the laser focal volume and a large sheath field at the target-vacuum interface is formed. This time-varying electric field effectively confines the majority of the hot electrons close to the target surface to form a disc expanding at close to the speed of light. The Ampére-Maxwell equation indicates an azimuthal magnetic field is associated with the radial expansion of the time-varying electric field. These fields have been measured and characterized using proton [29] and electron deflectometry [30]. The fields have strength of the order 100 MG contained within a thin layer close to the target surface and initially expand at close to the speed of light. Using these "relativistic" intensities to drive magnetic reconnection was recently investigated using copper K_α emission and magnetic spectrometers to diagnose the fast electrons [31]. Within the thin, hot plasma surface layer, where the magnetic fields are present, numerical modeling found the conditions to be such that the cold electron magnetization parameter $\sigma_{cold} = B^2/(\mu_0 n_e m_e c^2) > 1$. Extremely energetic astrophysical objects are also expected to have conditions considerably above this threshold.

To gain further insight into the relativistic electron driven reconnection experiments it is important to observe and then quantify the magnetic fields, however they are far more challenging to diagnose. The magnetic fields are present in a very narrow layer close to the target surface in densities close to the critical density for the laser pulses ($n_c = \epsilon_0 m_e \omega_L^2/e^2$, where ω_L is the laser frequency and m_e and e are the electron mass and charge respectively), making optical probing techniques such as Faraday rotation near-impossible. Proton deflectometry is the preferred method and can provide path integrated field maps. A proton beam is accelerated from a foil through the target normal sheath acceleration (TNSA) mechanism [32]. Therefore, to probe the magnetic fields of the reconnection geometry, two high-intensity laser pulses are required to drive the main interaction, as well as a third, high-energy, short-duration laser pulse to generate a time-resolving proton beam for probing the fields.

Currently, there are no facilities with three independent, high-energy, high-intensity beamlines and the flexibility to configure the experiment. However there are some facilities with two independent high-energy, picosecond-class pulses available, and significant setup flexibility, such as the Vulcan Target Area West (TAW) facility. Here we present an experiment performed at TAW, where one of the laser pulses is split into two foci that drive the main interaction and the other pulse drives the proton probe beam to enable magnetic field measurements of the relativistic electron driven reconnection experiment. A TNSA proton beam is used to measure the temporal dynamics of the path-integrated magnetic fields of the magnetic reconnection geometry. The analysis to achieve the field reconstructions are described in the appendices. The field strengths, likely magnetic field thickness and the dimensions of the reconnection layer are discussed.

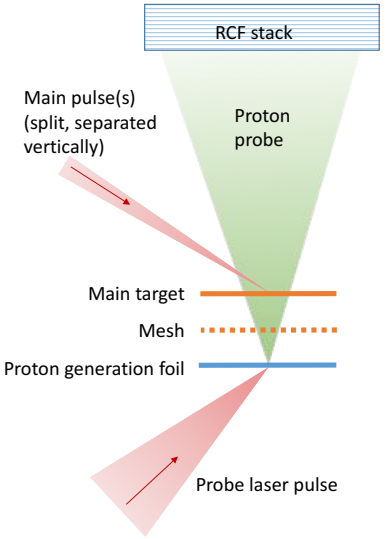

FIG. 1: A schematic of the experimental setup viewed from above.

II. EXPERIMENTAL SETUP

The TAW laser facility at the Rutherford Appleton Laboratory was used to perform the experiment. Two chirped pulse amplification (CPA) pulses are available; both have a central wavelength of 1.053 μm and are linearly polarized. The first CPA beam (main) was divided into two using a split mirror prior to the final focusing optic to produce the two, separated focal spots on the main target. The split mirror was adjustable so the relative timing could be altered for simultaneous arrival of the pulses on the target, as well as the relative angle between the two beams to produce the two laser focal spots at the interaction plane. An $f/15$ off-axis parabolic mirror produced full-width at half-maximum (FWHM) focal spots of 30 μm. The laser pulse duration was 9.6 ps and had a measured total laser beam energy (both laser foci) of (220 ± 27) J. For 87.4% energy transmission through the compressor [33], the peak on-target intensity would be 1.05×10^{18} Wcm^{-2}. The laser pulse had an angle of incidence onto the target of 45°. The main interaction targets were one of 4 different types of thin films; 30 μm thick polypropylene (PP), 10 μm or 25 μm thick copper or 15 μm thick aluminum.

The second beam (probe) was used to drive a TNSA [32] proton beam for use as a proton probing diagnostic. TNSA produces a proton beam with excellent properties for use as a probe of quasi-static electromagnetic fields [34]. The beams have a small virtual source size [35] and small emittance [36], providing excellent spatial resolution. They are accelerated on a timescale of approx-

imately the laser pulse duration meaning the temporal resolution is on the order of a picosecond [37]. The broad energy Maxwellian-like proton spectra means the beam becomes chirped due to the energy dependent time-of-flight from the source foil to the interaction, and a time-series of the interaction is produced in a single shot. Typically the proton probe is detected using a radiochromic film (RCF) stack and each RCF layer will approximately correspond to a narrow energy range of protons due to the Bragg peak in the proton stopping power, enabling the time series to be visualized.

An $f/3$ off-axis parabolic mirror focused the 1.6 ps duration, (89 ± 19) J pulse onto the 15 μm thick aluminum foil target at an angle of incidence of approximately 60° to generate the proton beam. This produced an elongated, elliptical focal spot with FWHM dimensions of 3.6 μm by 7.2 μm. Taking 63% energy transmission through the compressor [33], this corresponds to a peak intensity of 3.4×10^{20} Wcm^{-2}. The relative timing of the main interaction pulse to the probe pulse was varied using a delay stage before the compressor.

The rear projection proton probing geometry is illustrated in figure 1. The distance from the proton source foil to the main interaction target was 3 mm and the distance from the main interaction target to the front of the detector was 40 mm. This gave an approximate magnification of the interaction on the detector of 14. The detector was a RCF stack consisting of an aluminum foil light shield, and layers of HD-V2 films. A copper mesh, with a 63 μm pitch and a 25 μm thickness, was placed between the proton source and the main interaction at 1.5 mm from both foils.

While the hot electron temperature was not measured in the experiment, the temperature can be estimated from analytic and empirical scalings. Good agreement has been seen between measured hot electron temperatures in experiments utilizing high-intensity ($10^{17} - 10^{20}$ W/cm^2), picosecond-duration, moderate-contrast lasers, similar to the laser employed for these experiments. These are the Beg scaling [38],

$$T_{\mathrm{Beg}}[\mathrm{keV}] = 239 \left(\mathrm{I}\lambda_\mu^2/1.37 \times 10^{18}\mathrm{Wcm}^{-2}\right)^{1/3},$$

or the ponderomotive scaling [39],

$$T_{\mathrm{pond}}[\mathrm{keV}] = 511 \left(\sqrt{1 + \mathrm{I}_\mu\lambda^2/1.37 \times 10^{18}\mathrm{Wcm}^{-2}} - 1\right),$$

and they suggest a hot electron temperature between 170-220 keV for our experimental conditions. Therefore, the laser-heated electrons contributing to the interaction dynamics have a significant fraction of the electron rest mass energy with the distribution containing some relativistic electrons.

III. EXPERIMENTAL DATA

The main interaction target material was varied and example proton images for 10 μm thick copper, 15 μm thick aluminum and 30 μm thick polypropylene are shown in figure 2. Target material effects could manifest themselves in a few ways. The lower ionization threshold for lower Z materials could lead to different front side scalelength generated by the prepulse. This scalelength may both change the electron heating temperature and conversion efficiency as well as altering the expansion dynamics that lead to the formation of the magnetic fields. However, the higher Z material causes significant scattering, and hence blurring of the proton images, despite the thinner total thickness. The mesh structure is only visible in the images through the polypropylene target. SRIM [40] is used to estimate the average scattering angle of a 3.3 MeV proton through each target to be 59 milliradians for 10 μm thick copper, 39 milli-

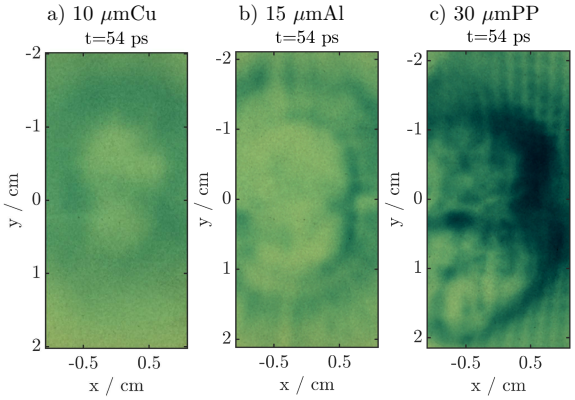

FIG. 2: Comparison of the raw proton probing images through the different materials. The laser focal spot separations are 430 μm. All of the RCF layers corresponds to a proton energy of 3.3 MeV and an approximate time after the leading edge of the main interaction pulses arriving at the target of 54 ps. The image contrast has been adjusted to enhance the proton beam structure.

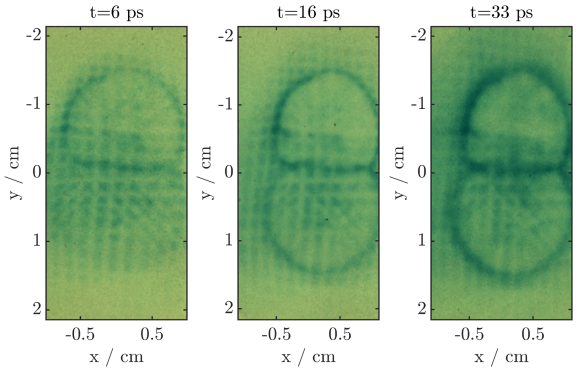

FIG. 3: RCF of the early time evolution of the proton deflectometry. The laser focal spot separation was 820 μm. The RCF layers, from left to right, correspond to proton energies of 5.6 MeV, 4.6 MeV, and 3.3 MeV. The image contrast has been adjusted to enhance the proton beam structure.

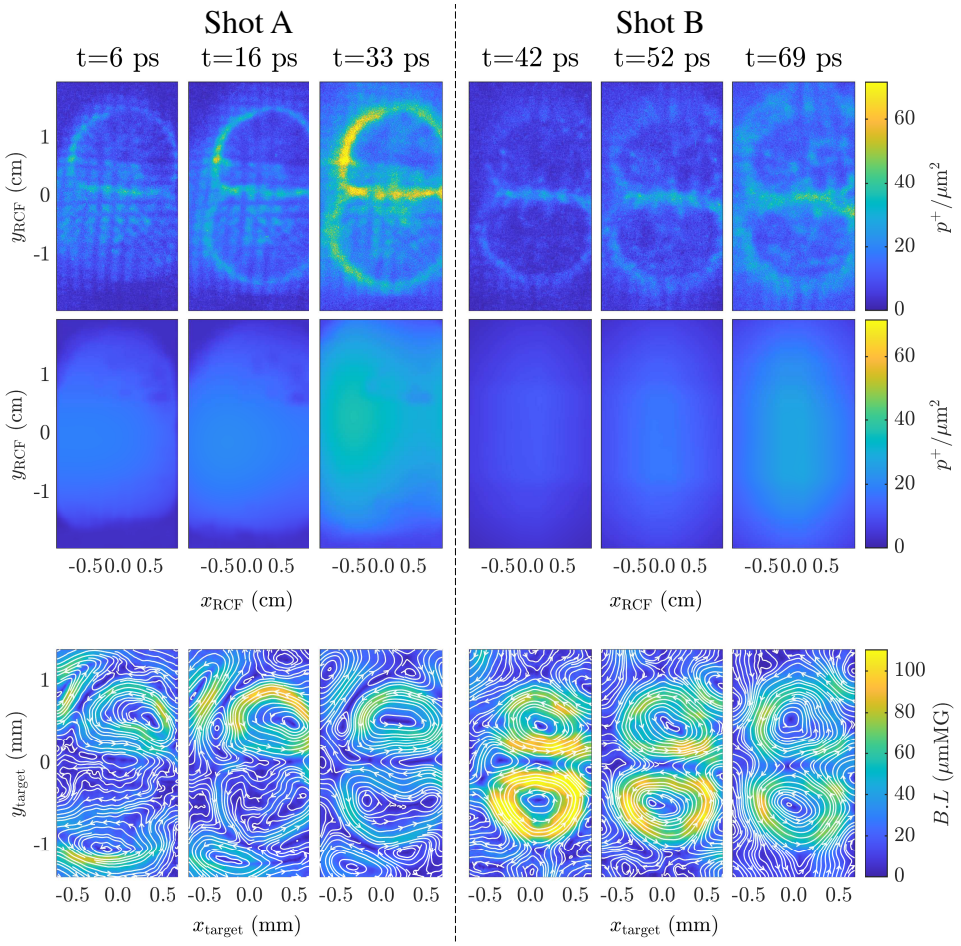

FIG. 4: Time series of magnetic field retrieval, showing the measured protons/μm^2 at the detector plane (top row), the calculated undisturbed beam flux at the detector plane (middle row) and retrieved path-integrated magnetic fields at the interaction plane (bottom row) for increasing time after arrival of the laser (left to right). The white contours with arrows show the topology of the calculated magnetic fields. The time series is composed of films from two separate shots, three early times from shot A (left) and three later times from shot B (right).

radians for 15 μm thick aluminum and 17 milliradians for 30 μm thick polypropylene. In the detector plane, this would blur the images to give spatial resolutions of about 170 μm, 110 μm and 50 μm respectively. The azimuthal magnetic fields generated by the two spatially separated, high intensity laser pulses interacted produces distortion of the fields from the purely circular fields observed around a single laser pulse.

In the metal targets the significant scattering of the proton beam makes quantitative retrieval of the fields challenging. Furthermore, the proton flux had considerable shot-to-shot variation meaning the proton flux and spatial distribution are not sufficiently stable to use as an unperturbed reference for the radiography calculation. However, two local reductions in the measured proton flux with flux enhancement at the edges are observed. These structures are noticeably smaller compared with those of the plastic targets taken at the same time and laser spot separation, with the smallest structures observed for the copper target. This implies that for this material the fields were either weaker, thinner (occupied a shorter path length along the proton trajectory) or their transverse extent smaller.

The scattering of the proton probe is minimize for the polypropylene target. Figure 3 shows the raw proton images for a polypropylene target where the focal spots are separated by 820 μm (shot A presented in figure 4). The times indicated are the time after the arrival of the leading edge of the main interaction pulses at the target.

To generate quantitative field measurements, these images are first processed, using the method described in Appendix A, to convert the scanned RCF images into number of protons. Then the proton data is processed using the field-reconstruction technique described in Appendix B to extract path integrated magnetic field maps using the Kugland image-flux relation and Ampére-Monge equation [41]. Appendix B describes the methods used to determine the undisturbed proton beam profiles,

a crucial step in the retrieval process. A masked 2D polynomial fit was used on for shot A to retrieve the field structures presented in figure 4 and a masked Gaussian fit was used for shot B. It is important to note that small discrepancies between the assumed undisturbed beam profile and the measured proton beam at the edges of the beam can lead to the retrieval of nonphysical magnetic fields. Also, although strong time-varying electric fields will be present during the interaction these are primarily directed normal to the target surface (along the direction of proton propagation) they should not contribute significantly to deflection of the protons. In this experiment, the proton beam dimension at the main interaction plane was a similar size to the features of interest, meaning the edge effects are particularly detrimental. We estimate the accuracy of the fields within the region of interest to have an error of $\sim$ 20%. Also the accuracy of the retrieved fields are strongly dependent on the overall flux and beam uniformity.

Figure 4 shows the evolution of the fields using data from two different shots. The absolute timings are given in reference to the first appearance of deformation within the proton beam in shot A, which was assumed to correspond to the arrival of the laser pulse. The first snapshot ($t = 6$ ps) likely illustrates fields driven during the 10 ps laser pulse duration, the later images follow the evolution of the fields. Shot B has a later timing for the proton beam and extends the temporal window to up to 69 ps with an estimated error of ± 1 ps. Note that shot B had 10% more energy in the main interaction laser pulses than shot A. The retrievals still produce much stronger fields for shot B compared to shot A. This could either indicate strong shot-to-shot variation, or the limited accuracy of the retrieval method based on the assumptions made to determine the magnetic field maps. The overall trend suggests an increase in field strength to a maximum shortly after the laser pulse with the maximum field strength decaying at later times.

Although the absolute magnitude of the fields retrieved is dependent on the choice of undisturbed beam and therefore has a large error we estimate to be $\sim$ 20%, and is perhaps affected by the curved 'beam'-front of the protons reaching the target, the qualitative shape of the fields is as expected, with the azimuthal fields around the focal spot disrupted in the region close to the second laser spot by the opposing azimuthal fields associated with that laser focus. The time series in figure 4 indicates strong fields generated during the first 6 ps of the interaction. The field-vectors also indicate the opposing direction magnetic fields in the midplane region required for magnetic reconnection.

The peak path integrated azimuthal magnetic fields retrieved here from the proton radiographs of the dual laser foci are in the region of 50–100 μmMG, and are of similar strength to those reported in measurements of single, relativistically-intense laser spots ($\sim 1\ \mu$m $\times$ 100 MG [30] and $\sim 10\ \mu$m $\times$ 40 MG [29]). Note these fields are much stronger than those typically measured from nanosecond duration laser interactions, where the magnetic fields are of the order 1 MG [16, 18].

In the absence of a measurement of the scale length of the magnetic field within the preplasma at the target surface, we have left the retrieved field in its path integrated form. It is tricky to estimate the likely front side scale length, l, since the target temperature and expansion will be highly dynamic over the temporal evolution of the laser pulse (relatively long at a FWHM of $\tau_L = 9.6$ ps). Using an isothermal expansion estimate, $l = c_s \tau_L$ [42],

$$l[\mu\mathrm{m}] \approx 0.3 \left(\frac{\mathrm{T_e}}{\mathrm{keV}}\right)^{1/2} \left(\frac{\mathrm{Z*}}{\mathrm{A}}\right)^{1/2} \left(\frac{\tau_\mathrm{L}}{\mathrm{ps}}\right)$$

with $T_e = 170$ keV, and for a pure proton plasma gives $l \approx 38\ \mu$m. However, this likely significantly overestimates the scalelength because the T_e is estimated from the peak intensity and the carbon component of the plasma will reduce the sound speed. Sarri et al., using the same laser system, with shorter pulse (1 ps), higher intensity (10^{19} Wcm^{-2}) found field thicknesses of 10 μm best matched their results [29]. Therefore an estimate of the path averaged field strengths in this experiment is made to be between $2 - 10$ MG.

Further information can be obtained from the reconstructed field images by considering the dimensions of the reconnection layer. The ratio of the width, δ, to the length, L, of the region can be used to determine the reconnection rate, the time it takes a magnetic field line to enter the diffusion region, reconnect and then exit the layer in the outflow plasma. For our retrieved magnetic fields, this ratio was estimated to be $\delta/L \approx 0.14$, using the FWHM of the best-fit Gaussian of the width, and defining the length of the region by the intersection point of the two bubbles. This is possibly an underestimate since the L is not FWHM as with δ. Raymond *et al.* observed $\delta/L \approx 0.3$ using copper K_α emission and numerical modeling in a similar regime [31]. It is, however, consistent with fast, collisionless reconnection which predicts rates of 0.1-0.2v_A [19].

Figure 5 shows lineouts of path integrated magnetic fields along the axis of symmetry perpendicular to the midplane for shot B. There are a couple of features to note. Firstly, the unsurprising observation that the magnetic field strengths decrease with increasing time. The fields persist for many pulse duration's ($\tau_L = 9.6$ ps), an observation that is consistent with Sarri *et al.* who made similar single spot measurements using $\tau_l = 1$ ps pulses [29]. Secondly, the relative strength of the magnetic fields decays quicker for the "internal" fields on both sides of the midplane region compared to the external fields on either side. This is likely because magnetic reconnection is taking place in the midplane region.

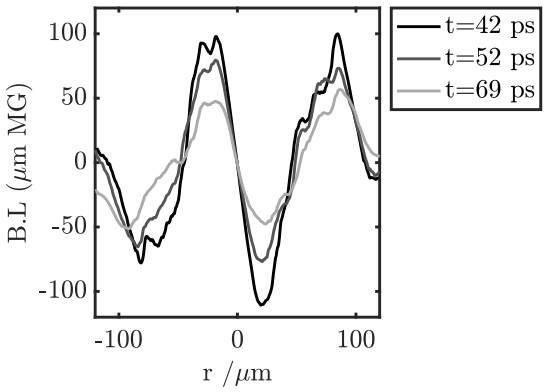

FIG. 5: $B_x L$ along the axis of symmetry of the magnetic fields for shot B shown in figure 4.

IV. SUMMARY

In conclusion, we have utilized proton radiography to probe the evolving azimuthal magnetic fields at the surface of thin targets of metal and plastic by two, co-timed, high intensity laser pulses. The data suggests reduced size fields on the metal targets in comparison with the plastic foils. An algorithm exploiting the Kugland image-flux relation together with the Monge-Ampére equation to retrieve the path-integrated magnetic fields assuming an initial proton flux distribution. As expected, two azimuthal fields were retrieved with field strengths up to $B \cdot L \sim 100$ μmMG. The field maps indicated the magnetic fields in the midplane were compressed and the field strengths reduce at a faster rate compared to the external fields. The width to length ratio of, $\delta/L \approx 0.14$, suggests a fast collisionless reconnection mechanism would be appropriate in this regime.

Future experiments could explore the differing field formation on metals and plastics in more depth utilizing higher energy proton probing. Finer temporal resolution in the design of the proton probing diagnostic would permit measurement of the rapid (6 ps) growth of the fields. With respect to using a field retrieval algorithm on TNSA proton radiography, the calculation of the assumed unperturbed proton beam is most successfully recreated using a custom 2D 3rd order polynomial or Gaussian filter, that is masked to recreate the beam edge. We note that using a larger distance between the source foil to the interaction, so that the proton beam overfills the region of interest would also improve the field reconstruction.

Appendix A: Radiochromic film characterization

Radiochromic film (RCF) is a dose dependent radiation detector that darkens on exposure to radiation. Used in a stack configuration, as was for this experiment, the film can be used to record the proton beam transverse profile for discrete proton energies. Following exposure, the films were scanned, after a wait-period of 24 hours, with a three color transmission scanner (Nikon CoolScan9000). The same device, and settings, were used to scan a set of calibration HD-V2 type films. These had previously been exposed, at the Birmingham synchrotron, to known doses of a 29 MeV proton beam between 0.1 and 200,000 Gy. The contributions of the three colour channels were combined and a custom fit used to obtain a pixel value to dose conversion.

Before conversion of the pixel values from raw data to dose, dark points due to the presence of dust on the films was removed. The dust removal method used was based on the technique developed by G. Hicks [43]. Here, a 2D-histogram of the pixel values of the green and blue channels is generated. Points that fall outside of $\pm 2.5\sigma$, where σ is the local rms of the distribution, are labelled as dust and the values are in-painted from the surrounding film. Since darker regions of film correspond to higher proton signal, and exclusion of regions of the film would affect the field retrieval algorithm, this step is very important.

Dose per pixel in Grays (1 G = 1 J/kg), is converted to energy per pixel by considering the density and volume of the active layer in which the proton energy is deposited. Here, density was assumed to be 1.2 gcm^{-3} [44] with the pixel volume of (84 $\mu\text{m}^2 \times 12\mu$m).

Conversion of energy deposited in the film in Joules to number of protons must consider that all protons with energies sufficiently high to reach a particular layer, will contribute to the deposited energy of that layer. This is illustrated in Figure 6, which shows response curves for the RCF stack, that is the energy deposited in each RCF layer as a function of initial proton energy (before entering the stack). These curves were calculated using proton stopping powers from SRIM [40] and a GUI developed by D. C. Carroll [45]. For the retrieval of the proton number, the signal on each layer is assumed to be due only to protons with energies falling within a bandwidth defined by deposition above $1/e$ of the maximum. The mean energy deposited by protons within this bin-width is used to estimate the number of proton in this energy bin from the deposited dose.

Typically, protons generated by TNSA exhibit a spectrum that decays exponentially with increasing proton energy up to the cut-off energy. By starting at the rear of the RCF stack, it is possible to remove the contribution of higher energy protons to pieces of film earlier in the stack. However, the absolute protons/pixel is important in determining how the proton flux at the stack has been locally affected by fields in the target. In order to correct the proton flux it is necessary to track the protons through the film so that the extra dose of higher energy protons is removed from the correct location in the earlier films. Due to the hundreds of micron (multi-pixel) positioning accuracy of the films relative to one another and the strong but spatially small flux modulation introduced by the mesh it was not possible to perform

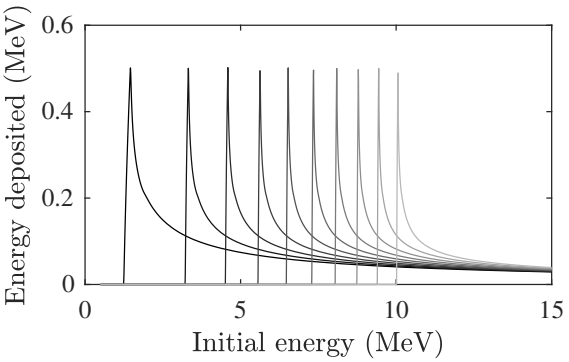

FIG. 6: Response curves of the RCF stack showing the energy deposited in each layer of the RCF stack by protons with different initial energies (darker lines for film layers at the front of the stack).

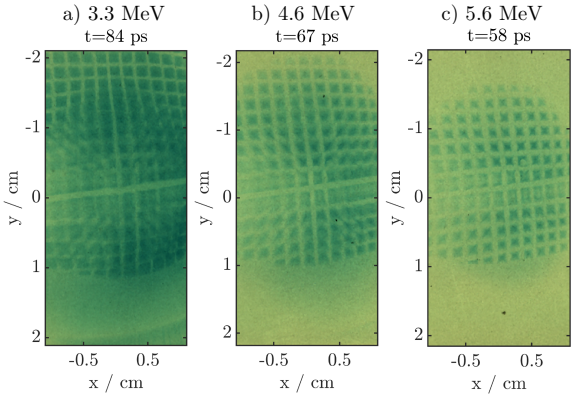

FIG. 7: Measure proton distributions for a) 3.3 MeV, b) 4.6 MeV and c) 5.6 MeV protons (the same energies as the films in figure 4) that have not interacted with the reconnection target. This illustrates the 'innate' distortion of the mesh.

this adjustment correctly. However, due to the typically exponential decay of the spectrum, the contribution of higher energy protons to each layer can be considered to be small. Since we are not concerned with the exact spectral shape, this contribution is negligible.

Appendix B: Magnetic field retrieval

Having converted the RCF film stacks into protons/pixel, it was then possible to study the local change in flux that is due to deflection of the protons in the electromagnetic fields of the plasma.

One technique that is commonly used to track the deflection of protons in the target fields is the introduction of a regular modulation into the proton beam prior to its passage through the target, e.g. a mesh. Distortion of this mesh can then be used to infer deflection of the protons relative to their initial trajectory. In the past this has been used to determine the fields generated around laser pulses and in moderate intensity reconnection experiments [8, 9, 11]. Here, the mesh was positioned between the proton source foil and the target at 1.5 mm from both. However, measurement of the proton beam in the absence of a reconnection target revealed distortion of mesh (figure 7). This distortion is more obvious at lower proton energies and complicates retrieval of the fields. It is likely to arise from the combination of multiple factors including; increased source size of the low energy protons and distortion of the target rear surface at late times, as well as charging and deformation of the mesh.

An alternative method to retrieve the path-integrated field is to consider the mapping of proton flux within the image as described in [46]. Here, we will follow the numerical model derived by Bott et al. in [41]. This model relates the proton flux distribution to the path-integrated magnetic field experienced during passage through the reconnection fields via an equation of Monge-Ampere type.

This method can provide a unique solution of the path-integrated field provided that there is no crossing of the protons within the beam (no caustics). The 'regime' of the probing is defined using the contrast parameter, μ (eqn. 1), which is related to; the distance from the proton source to the interaction, r_i; the interaction to proton detector, r_s; the magnetic field strength, B_{rms}; the proton 'speed', V; the length of the interaction plasma, l_z, and the correlation length of the magnetic field transverse to the proton propagation, l_B. The code was designed for use with stochastic magnetic fields for which the correlation length represented the typical scale length of the stochastic features. For the current problem, we calculate the contrast parameter by estimating the deflection angle, α, as the path integrated magnetic field along distance l_z. assume our fields will be of similar scale to the system size, l_z.

$$\mu = \frac{r_s r_i \alpha}{(r_s + r_i) l_B} = \frac{r_s r_i}{(r_s + r_i) l_B} \frac{e B_{rms} l_z}{m_p V} \approx 0.04 \qquad (1)$$

Here, we are safely within the non-linear regime ($\mu < 1$), in which there is still a unique mapping from initial beam to the line integrated magnetic field. In order to retrieve the fields, a number of assumptions need to be made. These are:

1. proton point source: the source size of our proton beam was not measured but can be assumed to be $< 20\mu$m as the mesh is clearly resolved.

2. point projection imaging: the distance from the interaction to the detector is 2-orders of magnitude larger than the size of the magnetic field along the proton path, meaning that the approximation $r_s \gg l_z$ is valid.

3. mono-energetic protons: although the proton beam itself has a broad energy spread, the proton energies contributing to each layer of the detector is

relatively small ($\Delta E/E < 10\%$). The contribution of a small range of proton energies to each layer will lead to low levels of 'blurring' in the flux distribution.

4. evolution of fields during proton passage through interaction: The duration of passage of mono-energetic protons through a 100 μm plasma is < 0.5 ps for all energies utilized here. While the evolution of the fields in a relativistic laser plasma interaction can be extremely rapid, the similarity of the images obtained for different probing times implies that our field structures are not evolving significantly over this timescale.

5. paraxial approximation: assuming a point source of protons at the proton foil, the half-angle divergence of the proton beam was calculated. This varies with proton energy from 9° to the maximum acceptance of the RCF stack (27°) implying that the proton beam cannot be approximated as planar at the interaction. This does not qualitatively change the contrast regime but can influence quantitative analysis.

6. initial proton profile: the proton beam profile is clearly non-uniform and estimation of this 'undisturbed' profile represents the largest source of error. This is discussed in greater depth below.

The basis of the field retrieval algorithm is that a change in flux distribution of the proton image results from local flux being redirected by the magnetic fields. Therefore a lack or excess of protons in a particular region can be used to infer the fields. This is only true if the undisturbed proton flux distribution is known. In many cases, for example capsule implosions, the undisturbed beam profile is isotropic and smooth and can be approximated by using the mean flux with any large-scale modulations estimated using a low-pass Fourier filter. In the case of TNSA-produced proton beams, this is not the case. The flux cut-off marking the 'edge' of the beam can have a strong gradient relative to flux variations within the beam. Shot-to-shot variability in beam profile and varying beam profile with proton energy, mean that it is difficult to infer the shape of the beam from 'reference' shots or RCF pieces corresponding to high energy/early time protons. In addition, in this case, the presence of the modulation imposed by the mesh adds an extra challenge since the frequency of this modulation is on a similar scale to the size of the signal and therefore Fourier filtering is ineffective.

In attempting to estimate the undisturbed proton flux profile, we have utilized a) flat mean-field, b) large sigma Gaussian filtering and c) 2D 3rd order polynomial fit. We present here the magnetic field retrievals for these methods. In figure 8, the different backgrounds are shown for the same film (figure 3c), together with the associated field-retrieval. It can be seen that in the case of the flat undisturbed beam (a), the beam edge, which is

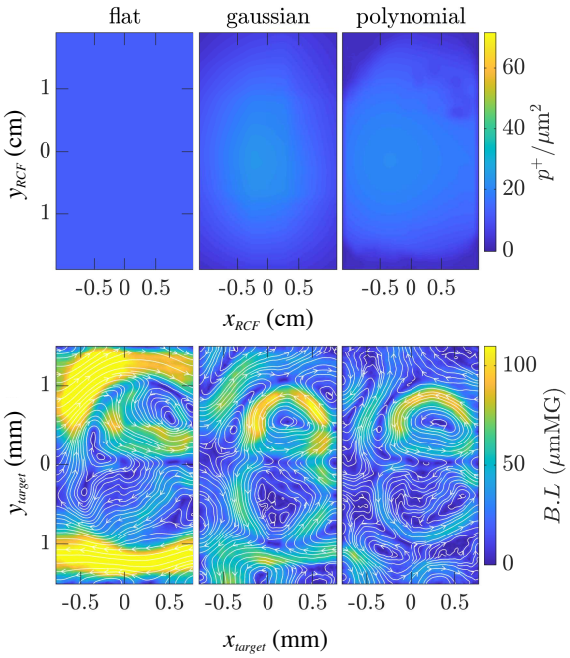

FIG. 8: Field retrievals (bottom row) at the interaction plane of $t = 33$ ps film in figure 4 using different assumed 'undisturbed' proton flux distributions shown at the detector plane (top row) including, from left to right, a flat mean-field, a σ =150-pixel Gaussian filter with 200-pixel kernal size, and a custom 2D 3rd-order polynomial, masked with the beam edge, in which the low flux regions are replaced with the original image.

not accounted for in the background, results in strong, non-physical fields. The algorithm deduces that the lack of flux in these regions compared with the flat distribution results from strong magnetic fields which dominate over the structure within the beam. The Gaussian filter (b) fairs better, with the gradual fall-off at the edge of the undisturbed beam reducing these spurious fields. However, in this case, the fall-off in flux is too gradual, such that in some cases there is a mismatch between the initial and final beam profile resulting in retrieval of non-physical fields.

In contrast, the masked 2D polynomial fit exhibits a much sharper drop-off in flux at the edge of the beam and more accurately follows the initial profile of the beam. This can be seen clearly in the central row of figure 4 which illustrates the undisturbed beam profile calculated using this custom polynomial for each of the different films within the same stack (the same shot). It is clear from the measured data that the beam edge is relatively sharp with changing beam size with proton energy. This custom fit, utilized a 2d 3rd-order polynomial fit to the measured data after the data had been smoothed with a large kernel Gaussian filter. This also leads to an overestimation of signal at the beam edge and so the fit was then masked to exclude values 'outside' the beam edge,

where the beam edge was defined as pixels with values falling below 25% of the measured maximum. The pixels outside of the edge of the beam were replaced with their values from the original data. This masked fit was then smoothed with a small (20-pixel) Gaussian filter to prevent sharp edges. As in all other cases, the total flux in the undisturbed image was adjusted to match the total flux within the measured image.

Acknowledgments

† Previous address: Physics Department, Lancaster University, Bailrigg, Lancaster LA1 4YW, UK, and The Cockcroft Institute, Keckwick Lane, Daresbury, WA4 4AD, UK. The authors gratefully acknowledge the support of the Central Laser Facility VULCAN engineering, laser and target area support teams. In particular the work of J. S. Green in making available characterized RCF and both P. L. Smith and J. Wragg for their efforts scanning the RCF. LW is supported by the National Science Foundation through Sponsor Award 1751462. We also acknowledge financial support from the STFC Cockcroft Institute Core Grant ST/G008248/1 for supplying the consumable diagnostics, and the Department of Energy National Nuclear Security Administration, under Award Number DE-NA0002727, for supporting our other US participants. The research also received partial funding from AWE plc., and the Engineering and Physical Sciences Research Council (grant numbers EP/M022331/1 and EP/N014472/1) of the United Kingdom.

[1] J. T. Gosling, Space Science Reviews, **172**, 187 (2012).
[2] Y. Lyubarsky, and J. G. Kirk, Astro. J., **547**, 437 (2001).
[3] B. F. Liu, S. Mineshige, and K. Ohsuga, Astro. J., **587**, 571 (2003).
[4] C. Thompson, Monthly Notices of the Royal Astronomical Society, **270**, 480 (1994).
[5] A. Balogh, M. W. Dunlop, S. W. H. Cowley, D. J. Southwood, J. G. Thomlinson, K. H. Glassmeier, G. Musmann, H. Lühr, S. Buchert, M. H. Acuna, D. H. Fairfield, J. A. Slavin, W. Riedler, K. Schwingenschuh, M. G. Kivelson, Space Sci. Rev., **71**, 5 (1997).
[6] J. A. Goetz, R. N. Dexter, and S. C. Prager, Phys. Rev. Lett., **66**, 608 (1991).
[7] M. Yamada, H. Ji, S. Hsu, T. Carter, R. Kulsrud, N. Bretz, F. Jobes, Y. Ono, and F. Perkins, Phys. Plas., **4**, 1936 (1997).
[8] P. M. Nilson, L. Willingale, M. C. Kaluza, C. Kamperidis, S. Minardi, M. S. Wei, P. Fernandes, M. Notley, S. Bandyopadhyay, M. Sherlock, R. J. Kingham, M. Tatarakis, Z. Najmudin, W. Rozmus, R. G. Evans, M. G. Haines, A. E. Dangor, and K. Krushelnick, Phys. Rev. Lett., **97**, 255001 (2006).
[9] C. K. Li, F. H. Séguin, J. A. Frenje, J. R. Rygg, R. D. Petrasso, R. P. J. Town, O. L. Landen, J. P. Knauer, and V. A. Smalyuk, Phys. Rev. Lett., **99**, 055001 (2007).
[10] P. M. Nilson, L. Willingale, M. C. Kaluza, C. Kamperidis, S. Minardi, M. S. Wei, P. Fernandes, M. Notley, S. Bandyopadhyay, M. Sherlock, R. J. Kingham, M. Tatarakis, Z. Najmudin, W. Rozmus, R. G. Evans, M. G. Haines, A. E. Dangor, and K. Krushelnick, Phys. Plas., **15**, 092701 (2008).
[11] L. Willingale, P. M. Nilson, M. C. Kaluza, A. E. Dangor, R. G. Evans, P. Fernandes, M. G. Haines, C. Kamperidis, R. J. Kingham, C. P. Ridgers, M. Sherlock, A. G. R. Thomas, M. S. Wei, Z. Najmudin, K. Krushelnick, S. Bandyopadhyay, M. Notley, S. Minardi, M. Tatarakis, and W. Rozmus, Phys. Plas., **17**, 043104 (2010).
[12] Jiayong Zhong, Yutong Li, Xiaogang Wang, Jiaqi Wang, Quanli Dong, Chijie Xiao, Shoujun Wang, Xun Liu, Lei Zhang, Lin An, Feilu Wang, Jianqiang Zhu, Yuan Gu, Xiantu He, Gang Zhao, and Jie Zhang, Nature Phys., **6**, 984 (2010).
[13] Quan-Li Dong, Shou-Jun Wang, Quan-Ming Lu, Can Huang, Da-Wei Yuan, Xun Liu, Xiao-Xuan Lin, Yu-Tong Li, Hui-Gang Wei, Jia-Yong Zhong, Jian-Rong Shi, Shao-En Jiang, Yong-Kun Ding, Bo-Bin Jiang, Kai Du, Xian-Tu He, M. Y. Yu, C. S. Liu, Shui Wang, Yong-Jian Tang, Jian-Qiang Zhu, Gang Zhao, Zheng-Ming Sheng, and Jie Zhang, Phys. Rev. Lett., **108**, 215001 (2012).
[14] M. J. Rosenberg, C. K. Li, W. Fox, A. B. Zylstra, C. Stoeckl, F. H. Séguin, J. A. Frenje, R. D. Petrasso, Phys. Rev. Lett., **114**, 205004 (2015).
[15] M. J. Rosenberg, C. K. Li, W. Fox, I. Igumenshchev, F. H. Séguin, R. P. J. Town, J. A. Frenje, C. Stoeckl, V. Glebov, and R. D. Petrasso, Nature Comms., **6**, 6190 (2015).
[16] J. A. Stamper, K. Papadopoulos, R. N. Sudan, S. O. Dean, E. A. McLean, and J. M. Dawson, Phys. Rev. Lett., **26**, 1012 (1971).
[17] J. A. Stamper, and B. H. Ripin, Phys. Rev. Lett., **34**, 138 (1975).
[18] C. K. Li, F. H. Se?guin, J. A. Frenje, J. R. Rygg, R. D. Petrasso, R. P. J. Town, P. A. Amendt, S. P. Hatchett, O. L. Landen, A. J. Mackinnon, P. K. Patel, V. A. Smalyuk, T. C. Sangster, and J. P. Knauer, Phys. Rev. Lett, **97**, 135003 (2006).
[19] W. Fox, A. Bhattacharjee, and K. Germaschewski, Phys. Rev. Lett., **106**, 215003 (2011).
[20] L. Willingale, A. G. R. Thomas, P. M. Nilson, M. C. Kaluza, S. Bandyopadhyay, A. E. Dangor, R. G. Evans, P. Fernandes, M. G. Haines, C. Kamperidis, R. J. Kingham, S. Minardi, M. Notley, C. P. Ridgers, W. Rozmus, M. Sherlock, M. Tatarakis, M. S. Wei, Z. Najmudin, and K. Krushelnick, Phys. Rev. Lett., **105**, 095001 (2010).
[21] A. Nishiguchi, T. Yabe, M. G. Haines, M. Psimopoulos, and H. Takewaki, Phys. Rev. Lett., **53**, 262 (1984).
[22] T. H. Kho and M. G. Haines, Phys. Rev. Lett., **55**, 825 (1985).
[23] A. S. Joglekar, A. G. R. Thomas, W. Fox, A. Bhattacharjee, Phys. Rev. Lett., **112**, 105004 (2014).
[24] P. Kolodner and E. Yablomovitch, Physical Review Letters, **43**, 1402 (1979)
[25] D. W. Forslund and J. U. Brackbill, Physical Review Letters, **48**, 1614 (1982)

[26] M. A. Yates, D. B. van Hulsteyn, H. Rutkowski, G. Kyrala, and J. U. Brackbill, Physical Review Letters, **49**, 1702 (1982)

[27] P. McKenna D. C. Carroll, R. J. Clarke, R. G. Evans, K. W. D. Ledingham, F. Lindau, O. Lundh, T. McCanny, D. Neely, A. P. L. Robinson, L. Robson, P. T. Simpson, C.-G. Wahlström, and M. Zepf, Physical Review Letters, **98**, 145001 (2007)

[28] C. P. Ridgers, M. Sherlock, R. G. Evans, A. P. L. Robinson, and R. J. Kingham, Physical Review E, **83**, 036404 (2011)

[29] G. Sarri, A. Macchi, C. A. Cecchetti, S. Kar, T. V. Liseykina, X. H. Yang, M. E. Dieckmann, J. Fuchs, M. Galimberti, L. A. Gizzi, R. Jung, I. Kourakis, J. Osterholz, F. Pegoraro, A. P. L. Robinson, L. Romagnani, O. Willi, and M. Borghesi, Phys. Rev. Lett., **109**, 205002 (2012).

[30] W. Schumaker, N. Nakanii, C. McGuffey, C. Zulick, V. Chyvkov, F. Dollar, H. Habara, G. Kalintchenko, A. Maksimchuk, K. A. Tanaka, A. G. R. Thomas, V. Yanovsky, and K. Krushelnick, Phys. Rev. Lett., **110**, 015003 (2013).

[31] A. E. Raymond, C. F. Dong, A. McKelvey, C. Zulcik, N. Alexander, A. Bhattacharjee, P. T. Campbell, H. Chen, V. Chvykov, E. Del Rio, P. Fitzsimmons, W. Fox, B. Hou, A. Maksimchuk, C. Mileham, J. Nees, P. M. Nilson, C. Stoeckl, A. G. R. Thomas, M. S. Wei, V. Yanovsky, K. Krushelnick, and L. Willingale, Phys. Rev. E, **98**, 043207 (2018).

[32] S. P. Hatchett, C. G. Brown, T. E. Cowan, E. A. Henry, J. S. Johnson, M. H. Key, J. A. Koch, A. B. Langdon, B. F. Lasinski, R. W. Lee, A. J. Mackinnon, D. M. Pennington, M. D. Perry, T. W. Phillips, M. Roth, T. C. Sangster, M. S. Singh, R. A. Snavely, M. A. Stoyer, S. C. Wilks, and K. Yasuike, Phys. Plas., **7**, 2076 (2000).

[33] D. C. Carroll, Private communication.

[34] M. Borghesi, A. Schiavi, D. H. Campbell, M. G. Haines, O. Willi, A. J. Mackinnon, P. Patel, M. Galimberti, and L. A. Gizzi, Rev. Sci. Inst., **74**, 1688 (2003).

[35] M. Borghesi, A. J. Mackinnon, D. H. Campbell, D. G. Hicks, S. Kar, P. K. Patel, D. Price, L. Romagnani, A. Schiavi, and O. Willi, Phys. Rev. Lett., **92**, 055003 (2004).

[36] T. E. Cowan, J. Fuchs, H. Ruhl, A. Kemp, P. Audebert, M. Roth, R. Stephens, I. Barton, A. Blazevic, E. Brambrink, J. Cobble, J. Fernández, J.-C. Gauthier, M. Geissel, M. Hegelich, J. Kaae, S. Karsch, G. P. Le Sage, S. Letzring, M. Manclossi, S. Meyroneinc, A. Newkirk, H. Pépin, and N. Renard-LeGalloudec, Phys. Rev. Lett., **92** 204801 (2004).

[37] J. Fuchs, P. Antici, E. D'Humières, E. Lefebvre, M. Borghesi, E. Brambrink, C. A. Cecchetti, M. Kaluza, V. Malka, M. Manclossi, S. Meyroneinc, P. More, J. Schreiber, T. Toncian, H. Pépin, and P. Audebert, Nature Physics, **2**, 48 (2006).

[38] F. N. Beg, A. R. Bell, A. E. Dangor, C. N. Danson, A. P. Fews, M. E. Hammel, B. A. Hammel, P. Lee, P. A. Norreys and M. Tatarakis, Physics of Plasmas, **4**, (1997).

[39] S. C. Wilks, W. L. Kruer, M. Tabak, and A. B. Langdon, **69**, 1383 (1992).

[40] J. F . Ziegler, M. D. Ziegler and J. P. Biersack, Nuclear Instruments and Methods in Physics Research Section B, **268**, (2010).

[41] A. F. A. Bott, C. Graziani, P. Tzeferacos, T. G. White, D. Q. Lamb, G. Gregori, and A. A. Schekochihin, Journal of Plasma Physics, **83**, (2017).

[42] W. L. Kruer, The Physics of Laser Plasma Interactions, Addison-Wesley, New York (1988).

[43] G. Hicks, PhD thesis: *Ion beams accelerated by laser irradiation of thin foils and their applications*, Imperial College London (2016).

[44] Aydarous, A. Badawi, and A. Abdallah, Results in Physics, **6**, 952 (2016)

[45] S. J. Millington, D.C. Carroll, and J.S. Green, Central Laser Facility Annual Report 2014-2015, page 48, (2015).

[46] N. L. Kugland, D. D. Rytov, C. Plechaty, J. S. Ross, and H. -S. Park, Review of Scientific Instruments, **83**, 101301, (2012).